1-1-2019

Multimodal Imaging And Asymmetry Of Disease Progression In Rhodopsin-Associated Autosomal Dominant Retinitis Pigmentosa

Lawrence Chan

Multimodal Imaging and Asymmetry of Disease Progression in Rhodopsin-associated Autosomal Dominant Retinitis Pigmentosa

A Thesis Submitted to the Yale University School of Medicine

in Partial Fulfillment of the Requirements for the Degree of Doctor of Medicine

by

Lawrence Chan

2019

Abstract

Retinitis pigmentosa (RP) is a group of genetically and clinically heterogeneous inherited retinal degenerative diseases with no known cure to date. The recent gene therapy treatment for Leber's congenital amaurosis and RP caused by mutations in *RPE65* have resulted in dramatic improvements in vision, leading to excitement for other potential gene therapies on the horizon. Upcoming clinical trials will be targeting patients with specific mutations, and measurements of disease progression will be needed for each genetic subtype of RP in order to determine whether treatments are successful. In this retrospective cohort study, we examined 27 RP patients with confirmed autosomal dominant mutations in the rhodopsin gene by monitoring rates of progression as measured structurally with ellipsoid zone (EZ) line width on spectral domain optical coherence tomography (SD-OCT), horizontal and vertical hyperautofluorescent ring diameters on short wavelength fundus autofluorescence (SW-FAF), and as measured functionally with 30 Hz flicker amplitudes on electroretinography (ERG). Each structural parameter was measured twice by the author four weeks apart. The mean rates of progression were -158.5 µm per year (-8.4%) for EZ line widths, -122.7 µm per year (-3.5%) for horizontal diameters, and -108.3 µm per year (-3.9%) for vertical diameters. High test-retest reliability was observed for the parameters (EZ line intraclass coefficient [ICC] = 0.9989, horizontal diameter ICC = 0.9889, vertical diameter ICC = 0.9771). The three parameters were also correlated with each other (r = 0.9325 for EZ line and horizontal diameter; r = 0.9081 for EZ line and vertical diameter; r = 0.9630 for horizontal and vertical diameters). No significant changes in ERG amplitude were seen. The subjects were classified by rhodopsin mutation class (I, IIa, IIb, III) and morphology of the hyperautofluorescent ring (typical vs. atypical). No significant differences in rates of structural progression were observed by rhodopsin mutation class or by ring morphology. Finally, higher rates of asymmetry of progression between the left and right eyes were detected for EZ line width (23% of subjects), horizontal diameter (17%), and vertical diameter (25%), as compared to studies on other forms of RP.

Acknowledgments

I would like to thank my mentors and thesis advisors Dr. Stephen Tsang and Dr. Ron Adelman for their mentorship and guidance with this project and my path through medicine and ophthalmology. I would also like to thank members of the Tsang lab for their invaluable assistance, including Dr. Ronaldo Carvalho for his help with planning the experimental design and Jimmy Duong for his much-needed statistical wizardry and patience with my incompetence. Furthermore, I also thank Dr. Ching-Hwa Sung from Weill Cornell Medicine for her expertise in biochemical characterization of rhodopsin mutations. I would like to express my gratitude to Dr. Ninani Kombo for her efforts in helping me with the revision process. I also want to show my deepest appreciation to the Yale Department of Ophthalmology and Visual Science, especially to Deana Ralston for her incredible guidance with finalizing the thesis. I thank my wonderful friends, classmates, mentors, and family for their unending support for as long as I can remember. Finally, I want to thank my fiancée and life partner Yue Meng for her unconditional love and guidance at every step of my life these past seven years.

Table of Contents

Introduction

Retinitis pigmentosa (RP), a group of inherited retinal diseases with an incidence of approximately one in 4000 people, is characterized by progressive photoreceptor death and irreversible vision loss (1). Typically, the initial loss of photoreceptors primarily involves the rods, thereby diminishing peripheral and night vision, followed by worsening tunnel vision and eventual loss of central vision mediated by cone photoreceptor death (1). Ophthalmoscopic hallmarks of the disease include retinal arteriolar attenuation, bone-spicule peripheral pigment deposits, and waxy pallor of the optic disc (2). The clinical presentation of retinitis pigmentosa is highly variable. The severity and pattern of vision loss may be mild or severe. The rate of disease progression can be slow or rapid, and the age of onset can be as early as childhood while some individuals remain asymptomatic until mid-adulthood. Allelic heterogeneity, in which each gene locus may have different mutations that cause the same disease entity, contributes to the diverse genetic etiology of RP; for example, over 300 different *RPGR* mutations have been identified in families with X-linked RP (3). Even among members of the same family, the same mutation may result in different phenotypic manifestations. RP is also a genetically heterogeneous disease, with over 50 genes that have been found to be associated with non-syndromic RP. Further complicating the heterogeneity of the disease is that different mutations in the same gene may result in different modes of inheritance. The pattern of inheritance can be autosomal recessive (15-20%), autosomal dominant (20-

25%), X-linked recessive (10-15%), or sporadic (30%) (2, 4). RP may also be syndromic, as seen in Bardet-Biedl syndrome, Usher syndrome, abetalipoproteinemia (Bassen-Kornzweig syndrome), and phytanic acid oxidase deficiency (Refsum disease) (2).

Despite the genetic complexity of RP, improvements in the cost and efficiency of molecular techniques that allow for the high-throughput DNA sequencing of patients have resulted in clinicians being able to append a molecular diagnosis to their clinical diagnosis. Specifically, the advent of next-generation sequencing (NGS), which is able to perform massively parallel sequencing runs on the order of millions of DNA fragments using micron-sized beads, has dramatically increased the speed of sequencing many-fold and enabled the capture of a broader spectrum of mutations compared to conventional Sanger sequencing (5).

Molecular basis of the visual cycle

To understand how mutations in certain genes may cause RP, an outline of the visual cycle will need to be described. The first step in vision occurs when light enters the eye and is focused by the cornea and lens onto the retina (photosensitive tissue located posteriorly within the eye). In the retina, the light-sensitive photoreceptor cells called rods and cones convert the external light stimuli into electrical impulses that the brain processes to form an image. Rod photoreceptors contain the visual pigment rhodopsin, which is a light-sensitive G-

protein coupled receptor that consists of the apoprotein opsin and 11-*cis*-retinal, a chromophore. When light is absorbed by rhodopsin, the 11-*cis*-retinal is converted to all-*trans*-retinal and leads to a series of conformational changes of the opsin that activates the GTP-binding protein transducin, triggering a canonical cyclic guanosine monophosphate (cGMP) second-messenger cascade through the activation of cGMP phosphodiesterase (PDE) (2). PDE hydrolyzes cGMP, leading to closure of the cGMP-dependent cation channels normally responsible for influx of Na^{+}, Ca^{2+}, and Mg^{2+}. The resulting hyperpolarization of the photoreceptor cell decreases the rate of transmitter release and elicits responses in second-order (bipolar) cells for further neural transmission (6). The all-*trans*-retinal is converted to all-*trans*-retinol and is transported to the retinal pigment epithelium (RPE) to be recycled into 11-*cis*-retinal for transport back into the rods (2).

Rods are sensitive to low levels of light, and psychophysical experiments have shown that they can register single photon absorptions (6). Since rods play a crucial role in enabling vision in low-light scenarios and are anatomically located in the periphery of the retina, RP patients usually experience night blindness (nyctalopia) and loss of peripheral vision as their initial symptoms.

The organization of the rod photoreceptor consists of a synaptic body that interfaces with the bipolar/horizontal cells, a cell body, an inner segment (IS) which contains the endoplasmic reticulum, mitochondria, and Golgi apparatus,

and an outer segment (OS) which houses membranous discs containing mostly opsin within a plasma membrane. The IS and OS are connected by the connecting cilium, and the OS interfaces with and is phagocytosed by the RPE.

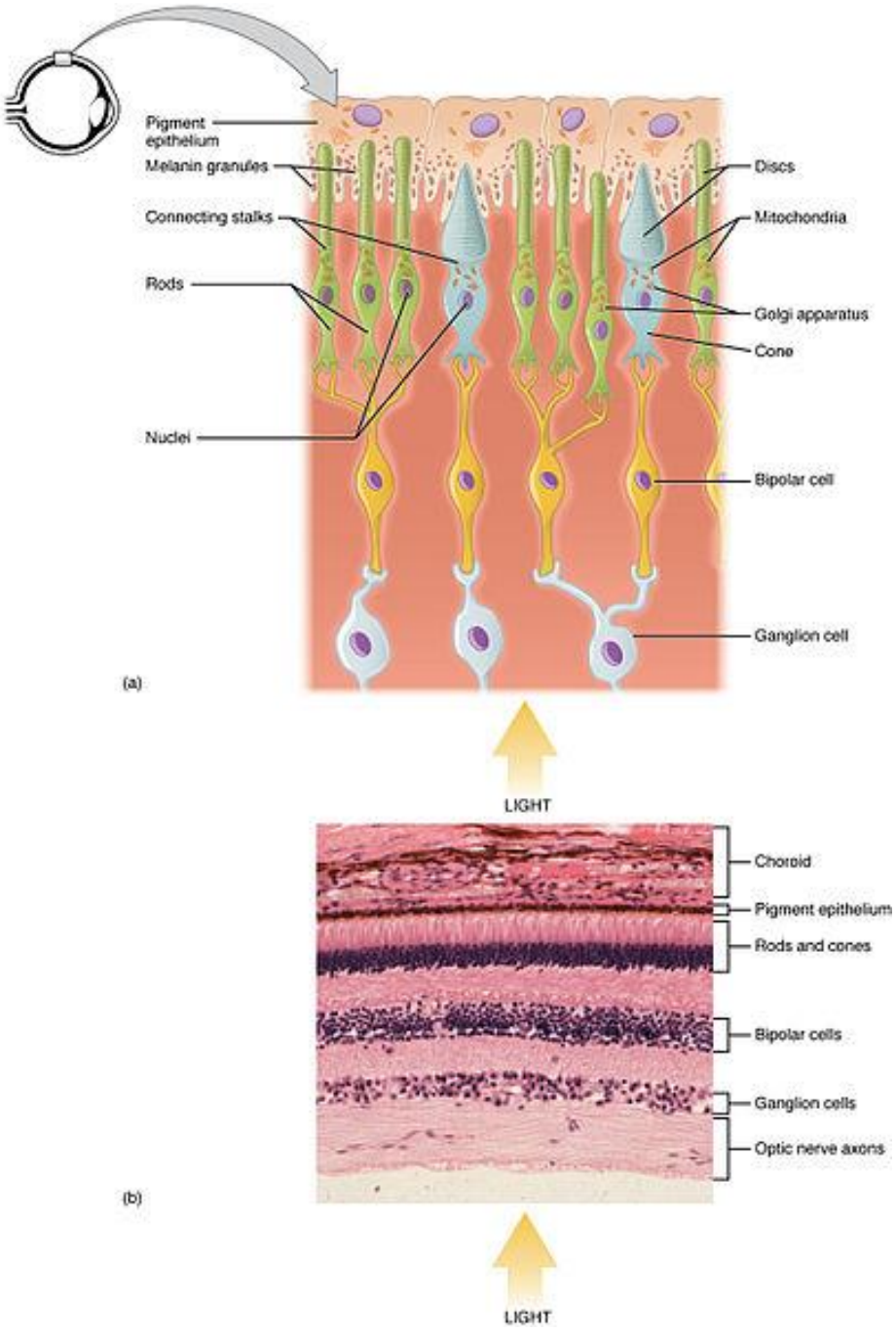

Figure 1. a) Illustration showing cell organization within the retina. b) Cross-sectional H&E stain of retina. Image from Wikimedia Commons.

Structure of rhodopsin

As previously mentioned, rhodopsin (RHO) is the G-protein coupled receptor (GPCR) that is responsible for the first step in allowing rod photoreceptors to detect light. It is synthesized in the rough endoplasmic reticulum and then transported through the Golgi apparatus where it ultimately functions within the discs of the OS (7). 30% to 40% of all autosomal dominant RP (adRP) is caused by mutations in the *RHO* gene, and over 120 different mutations in *RHO* have been identified (2, 8). One study of 200 families with clinical evidence of adRP found that rhodopsin mutations were the most common cause of disease, representing 26.5% of the total cases of adRP (9). In addition to its role in adRP, rhodopsin was the first GPCR whose crystal structure was elucidated, and it served as a prototype template for understanding the rest of the GPCR superfamily (8). Rhodopsin is a highly conserved protein among vertebrate species, and similar proteins have even been found in the visual systems of invertebrates such as *Drosophila melanogaster* (10). The structure of rhodopsin consists of four specialized domains that assist in the maintenance of protein structure, trafficking, and phototransduction: 1) cytoplasmic, 2) intradiscal, 3) transmembrane, and 4) ligand-binding domains (11). The cytoplasmic C-terminal domain of rhodopsin regulates its trafficking and interactions with other proteins in the phototransduction cascade such as transducin (11). The intradiscal domain contains the extracellular loops between transmembrane domains and the N-terminus. Research suggests that mutations in the intradiscal domain result in

misfolding of the protein and accumulation of the protein within the secretory system, leading to disease (12). The transmembrane domains have been shown to have several residues that are important for rhodopsin protein stability and function (13). The ligand-binding domain is where the 11-*cis*-retinal chromophore binds with the opsin apoprotein (14).

Biochemical classification of rhodopsin mutations

Mutations in rhodopsin causing adRP have been grouped into three classes (Table 1) based on the phenotypes of the proteins from *in vitro* studies that transfected human tissue culture cells with wild-type and mutant rhodopsin cDNA clones (8, 11, 12). Class I mutations are located near the C-terminus of the protein or within the first transmembrane segment. The protein resembles wild-type rhodopsin in terms of protein levels, ability to associate with the 11-*cis*-retinal chromophore, and subcellular localization (15, 16). However, these mutations cause rhodopsin to activate transducin inefficiently in the presence of light (17). Class II mutations cause decreased binding to 11-*cis*-retinal and result in accumulation within the endoplasmic reticulum, possibly due to issues with protein folding and stability (15, 17). Within class II, further subclassification can be made for those mutants that predominantly localize intracellularly (class IIa) and those that preferentially localize to the cell surface (class IIb) (16). Finally, class III mutants form rhodopsin poorly and at low levels, are retained in the endoplasmic reticulum, and may form aggresomes, causing targeted degradation

by the ubiquitin proteasome system (18). Studies have suggested that impaired endocytic activity is the primary mechanism by which class III mutations cause RP (19). One common finding among all three classes of mutations is the decreased sensitivity to light and less efficient activation of transducin (17).

Table 1. Classification and description of rhodopsin mutants

Class	Biochemical phenotype
I	Mutations occur near C-terminus Similar to wild-type rhodopsin Inefficient activation of transducin
II	Misfolding/instability Accumulation within endoplasmic reticulum Class IIa: localize intracellularly Class IIb: localize to cell surface
III	Impaired endocytosis from membrane Form rhodopsin chromophore poorly Accumulation within endoplasmic reticulum

Clinical classification of rhodopsin patients

Aside from the preceding classification of rhodopsin mutations based on biochemical characteristics, research on adRP caused by rhodopsin mutations has produced evidence of two different subtypes predicated on the clinical pattern of disease. The class A phenotype, sometimes referred to as “type 1” or “diffuse” subtypes, is characterized by a severe, early-onset diffuse loss of rod sensitivity with a later prolonged degeneration of cones (20, 21). The class B phenotype, also known as “type 2” or “regional”, exhibits a combined loss of rod and cone sensitivity in a superior hemifield (altitudinal) pattern with relatively preserved function in the inferior hemifield, as well as a slower progression of

disease with night blindness manifesting during adulthood (21). Because of the regionalized retinal degeneration in the altitudinal pattern, these phenotypic variants of RP are also known as sector RP (22). It has been postulated that the more severe class A phenotype may be caused by a gain-of-function mutation that is cytotoxic, while the milder class B phenotype is a result of a loss-of-function mutation inherited on a single allele (23).

Potential for therapeutic intervention

Gene therapy is an experimental technique that seeks to treat genetic disorders by replacing or supplementing the mutated gene with a healthy copy of the gene, or inactivating a mutated gene, in contrast to traditional therapies such as surgery and medications. In late 2017, Spark Therapeutics' LUXTURNA™ (voretigene neparvovec), a treatment for LCA and RP caused by mutations in the *RPE65* gene, became the first gene therapy for any disease to gain regulatory approval in the United States by the Food and Drug Administration. This gene therapy involves the subretinal injection of wild-type copies of *RPE65* packaged in an adeno-associated virus (AAV).

RPE65 (retinal pigment epithelium-specific protein, 65 kDa) is responsible for producing the isomerase enzyme that catalyzes the isomerization of all-*trans*-retinal back to 11-*cis*-retinal within the retinal pigment epithelium so that the previously mentioned visual cycle can begin again (24). In LCA and RP caused

by bi-allelic mutations in *RPE65*, the visual cycle is disrupted and photoreceptors undergo dysfunction and degeneration, the two pathological mechanisms that ultimately lead to progressive blindness (25). Early preclinical studies in mouse and dog models have shown that gene augmentation therapy is able to correct the biochemical blockade and result in significant, persistent vision improvement (25). These promising initial results over the past two decades led to the University of Pennsylvania research group to collaborate with Spark Therapeutics to test the efficacy and safety of AAV2-hRPE65v2 (voretigene neparvovec) on 31 patients across two leading US academic centers for the study of inherited retinal dystrophies (Children's Hospital of Philadelphia, Philadelphia, PA and University of Iowa, Iowa City, IA). This randomized controlled study, the first phase 3 trial for any gene therapy, demonstrated clinically and statistically significant improvements in the subjects' visual field measurements and ability to independently navigate in low-light conditions, persisting throughout the one-year follow-up period (26).

The success of the *RPE65* gene therapy trials has spawned a large number of clinical trials seeking to use gene therapy to cure other inherited retinal degenerative diseases. For example, there are several endeavors in the US and the UK to study gene therapy treatments for choroideremia, an X-linked recessive retinal disease that causes progressive loss of peripheral vision and night blindness (27, 28). Choroideremia is caused by mutations in the *CHM* gene, which encodes for the Rab escort protein-1 (REP1). This condition is

amenable to treatment with gene therapy using an adeno-associated virus 2 (AAV2) capsid due to the relatively small size of the *CHM* cDNA payload that can be contained with the AAV2 vector (28).

However, unlike the loss-of-function mutations of the recessive choroideremia and LCA that can be addressed with simple replacement of the wild-type gene, RP caused by a dominant *RHO* mutation acquires an abnormal gain of function that requires suppression of the mutant *RHO* gene and replacement with the wild-type version. Strategies for suppressing the toxic gene include transcriptional silencing, RNA interference, and ablation or correction of the mutation at the DNA level using gene editing techniques such as zinc finger nucleases (ZFNs), transcription activator-like effector-based nucleases (TALENs), and the recently discovered clustered regularly interspaced palindromic repeats (CRISPR)/Cas9 system. For *RHO*-adRP specifically, efforts over the past few decades have focused on either targeting specific mutant alleles for reduction in expression levels or by implementing a mutation-independent knockdown strategy (29-31). The mutation-independent strategy is particularly useful given the heterogeneity of the disease due to the large number of disease-causing *RHO* mutations. This generally involves silencing the expression of both the mutant and wild-type *RHO* alleles, while supplementing wild-type protein-encoding *RHO* cDNA that is modified to be resistant to the suppressor. Various methods exist to silence gene expression, including RNA interference (RNAi) via short hairpin RNA (shRNA) or small interfering RNA

(siRNA), CRISPR/Cas9, and TALENs (32). One way of conferring resistance to the replacement *RHO* cDNA is to modify codons to contain wobble nucleotides at the target site, thereby decreasing hybridization with the suppressor reagent (33).

The goal of finding treatments that are targeted to each specific genetic disorder is timely given the launch of the United States Precision Medicine Initiative during President Barack Obama's tenure. There has been an increased interest among the scientific and medical communities to discover "precision medicine" treatments tailored to each individual's variability in genes, environment, and lifestyle (34). Given the inevitable progress within the next decade in the field of gene therapy in the wake of LUXTURNA, there is a crucial obligation to characterize the natural history progression of each disease on a gene-by-gene basis. Without baseline measurements of disease progression rates and asymmetry between eyes, it will be difficult to determine the efficacy of retinal gene therapy even with an untreated control eye.

Structural and functional assessments

Various structural and functional measures of disease severity exist within the field of ophthalmology. Visual acuity and visual field testing are able to capture the patient's perception of visual impairment, but they are subjective tests that have low test-retest reliability (35, 36). An objective method of assessing visual function is electroretinography (ERG). This noninvasive electrophysiologic test of

retinal function uses recording electrodes placed on the corneal surface and measures the changes in electric potential (against a reference electrode placed on the skin) in response to light stimuli of varying intensities under dark- and light-adapted conditions. The stimulation of the retina produces characteristic waveforms that provide information about the function of different cells within the retina, such as rods, cones, bipolar cells, retinal ganglion cells, and amacrine cells. Important parameters of the waveform include the a- and b-wave amplitudes (distance from baseline to a-wave trough, and from a-wave trough to b-wave peak, respectively) and implicit time (time between stimulus onset and maximum amplitude). The ERG is a useful tool in diagnosing many retinal conditions, including retinitis pigmentosa, congenital stationary night blindness, achromatopsia, toxic retinopathies, and cancer-associated retinopathy (37). It also has utility in objectively assessing the retinal function in animal research models. There are different forms of ERG, such as the standardized full-field ERG (ffERG) which measures the total retinal response, pattern ERG (PERG) which assesses central retinal function, and the multifocal ERG (mfERG) which can detect localized responses in precise regions of the retina within the central 30 degrees (38). ERGs have shown increased reproducibility of measurements compared to visual field testing, but are limited in their ability to reliably detect small variations such as in end-stage retinal disease (35).

Imaging modalities such as spectral-domain optical coherence tomography (SD-OCT) and fundus autofluorescence (FAF) have also been shown to be practical

tools in providing data about retinal and RPE structures that correlate well with disease progression and functional measures (39). With the loss of photoreceptors in the periphery that gradually progresses towards the fovea seen in RP, it is important to be able to visualize and differentiate between the dysfunctional, diseased portions and the healthy viable regions of the retina. One visual marker of this border is the parafoveal ring of increased autofluorescence first shown to be correlated with PERG by Robson et al. in 2003 (40). The short-wavelength autofluorescence (SW-AF) imaging technique uses blue light excitation at 488 nm and detects signals originating from lipofuscin granules and other fluorophores within the RPE/photoreceptor complex (41). In RP patients, these signals may manifest as rings and are thought to be the transition between healthy and diseased retinal areas, with normal function within the ring and dysfunction outside the ring (42). Some researchers have theorized that the increased intensity of the autofluorescence signal is due to atrophy or stress-induced accumulation of lipofuscin – the oxidative byproduct of phagocytosed photoreceptor outer segments – within the RPE (43). The maximum intensity of the signal captured by FAF may therefore represent the distribution of active degeneration of photoreceptors where there is a high rate of phagocytosis by the RPE; dark areas seen on fundus autofluorescence are indicative of atrophy of the RPE and corresponding loss of lipofuscin granules (44). Studies have demonstrated that the rate of hyperautofluorescent ring constriction is correlated with visual field loss progression and has prognostic value in predicting visual field acuity and visual field preservation (45).

In addition to FAF, SD-OCT is another noninvasive imaging modality that can allow for *in vivo* visualization of the retinal layers. One hyperreflective band layer that can provide information about photoreceptor health and function is the ellipsoid zone (EZ), previously known as the inner segment/outer segment (IS/OS) line (though the precise anatomic origins continue to be a topic of debate). The hyperreflectivity of the EZ likely corresponds with the light scattering by the mitochondria within the distal portion of the inner segment (46). Disruption and/or shortening of the EZ line width corresponds with loss of visual field sensitivity and thus provides a structural marker for the visual field edge (47, 48). Some studies have shown that measurement of the EZ line width may be more sensitive than full-field ERG and standard visual field testing in detecting progression of visual field changes in RP. Birch et al. found that the rate of change in EZ line width is consistent with those reported for ERGs and visual fields, yet the test-retest variability of the EZ line width was considerably lower (39). Furthermore, Birch et al. showed that the edge of the EZ line is where the visual field sensitivity changes most accurately, and that observing this region is more sensitive in detecting disease progression than global measurements that average across the entire field (i.e., monitoring the healthy macula and the diseased periphery, which are relatively stable) (49).

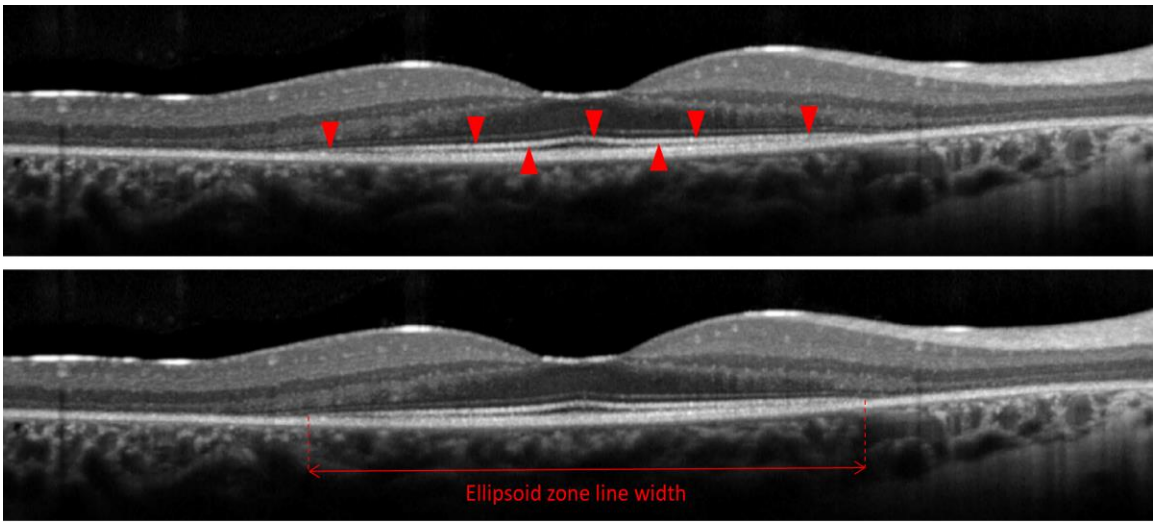

Figure 2. SD-OCT image showing retinal layers. Red arrow heads pointing to ellipsoid zone line layer (top). Measurement of ellipsoid zone line width between dotted lines (bottom).

Statement of Purpose

Retinitis pigmentosa (RP) is a group of inherited retinal degenerative diseases affecting roughly one in 4000 people worldwide and manifests as a progressive loss of vision. The pattern of visual loss generally involves the initial degeneration of the rod photoreceptors, followed by loss of the cones. It is marked by clinical and genetic heterogeneity, with varying rates of vision loss and levels of disease severity, different modes of inheritance, and more than 100 genes whose mutations have been found to cause RP. There is currently no known cure for RP, but the recent groundbreaking FDA-approved gene therapy treatment (LUXTURNA™) for Leber's congenital amaurosis and RP caused by mutations in *RPE65* has shown dramatic improvements in vision and given promise that gene therapy is a viable strategy for treating inherited retinal diseases.

For future gene therapy clinical trials, it will be crucial to have data regarding RP natural disease history and appropriate outcome measurements on a gene-by-gene basis given the heterogeneity of the disease. Furthermore, precise details about disease severity based on the various types of mutations within a single gene would inform researchers about their decisions to enroll patients with certain mutations. In this study, we seek to examine a subset of autosomal dominant RP patients with known mutations in the rhodopsin gene (*RHO*) using structural (ellipsoid zone line width, hyperautofluorescent ring diameters) and functional (electroretinography) assessments to monitor disease progression. We will also look for asymmetry of rates between eyes and any correlations between the rhodopsin mutation class, morphology of the hyperautofluorescent ring, and disease severity.

Methods

Subjects

This study was conducted in adherence to the tenets of the Declaration of Helsinki. All study procedures were defined and approved by the Institutional Review Board at the Edward Harkness Eye Institute and Columbia University Medical Center (Protocol #AAAR0284). Patient consent was obtained from all subjects. The patient data presented here, including images and genetic testing results, are not identifiable to individual patients. Diagnoses of RP were made by an inherited retinal disease specialist (S.H.T.) based on clinical history, fundus examinations, and full-field electroretinography (ffERG) results. This is a retrospective cohort study with the following inclusion criteria: 1) patients must have genetic sequencing-confirmed RHO mutations; and 2) a complete ophthalmic examination must have been performed by our retinal disease specialist on at least one visit. Since our clinic is an international referral center for patients with RP, a significant portion of the subjects had their care transferred back to their primary provider after the initial diagnosis was made in our clinic using imaging, electroretinography, and genetic testing and thus did not return for a follow-up visit. Patients were excluded if they: 1) presented with advanced stage RP with no visible ellipsoid zone line in any eye at all time points; 2) had unilateral RP; 3) did not have any visible hyperautofluorescent ring in any eye at all time points; and 4) had poor image quality. A total of 38 patients fit our inclusion criteria; 11 patients were excluded based on the exclusion

criteria, leaving a total of 27 patients on whom to base our analysis. The 38 patients belonged to 21 different families; the final 27 subjects belonged to 18 different families. For the 27 patients who were studied, eyes were analyzed only if there were visible EZ lines/hyperautofluorescent rings; if there were no EZ lines/hyperautofluorescent rings, the eye at that time point was not included.

Genetic analysis

DNA was extracted from the blood obtained from patients and was tested for previously published RP genes of the Chiang panel at Columbia University Medical Center Department of Pathology and Oregon Health Sciences University. Parallel sequencing was performed using the Illumina HiSeq platform with 100 bp paired-end reads, and mutations were confirmed by dideoxy chain-terminating sequencing.

Mutation classification

Each patient was assigned a biochemical rhodopsin mutation classification based on PubMed literature searches for each specific mutation. Biochemical classifications were found for 32 out of 38 patients. Patients 3 and 4 had mutations that have not been studied and classified. For patients 6-9, the mutations were studied in bovine rhodopsin and were not characterized using the

classification system proposed by Sung et al. (16, 50, 51). Table 2 lists the mutation classifications as well as their corresponding literature references.

Table 2: Rhodopsin biochemical mutation classification, including excluded patients

	Genotype	Mutation class	Reference
1	RHO (c.556T>C:p.Ser186Pro)	IIa	PMID8253795
2	RHO (c.937-27_-19delCCCTGACTC)	I	PMC52606
3	RHO (c.946delT:p.Cys316Alafs*44)	-	
4	RHO (c.946delT:p.Cys316Alafs*44)	-	
5	RHO (c.266G>A:p.Gly89Asp)	IIb	PMC52606
6	RHO (c.83A>G:p.Glu28Arg)	-	
7	RHO (c.328T>C:p.Cys110Arg)	-	
8	RHO (c.328T>C:p.Cys110Arg)	-	
9	RHO (c.328T>C:p.Cys110Arg)	-	
10	RHO (c.568G>A:p.Asp190Asn)	IIa	PMID8253795
11	RHO (c.568G>A:p.Asp190Asn)	IIa	PMID8253795
12	RHO (c.266G>Ap.Gly89Asp)	IIb	PMC52606
13	RHO (c.1025G>A:p.Thr342Met)	I	PMC52606
14	RHO (c.541G>A:p.Glu181Lys)	IIa	PMID8253795
15	RHO (c.800C>T:p.267Leu)	IIa	PMID8253795
16	RHO (c.316G>A:p.Gly106Arg)	IIb	PMID8253795
17	RHO (c.404G>T:p.Arg135Leu)	III	PMC437971
18	RHO (c.1040C>T:p.Pro347Leu)	I	PMC52606
19	RHO (c.1040C>T:p.Pro347Leu)	I	PMC52606
20	RHO (c.1040C>T:p.Pro347Leu)	I	PMC52606
21	RHO (c.1040C>T:p.Pro347Leu)	I	PMC52606
22	RHO (c.1040C>T:p.Pro347Leu)	I	PMC52606
23	RHO (c.1040C>T:p.Pro347Leu)	I	PMC52606
24	RHO (c.1040C>T:p.Pro347Leu)	I	PMC52606
25	RHO (c.800C>T:p.267Leu)	IIa	PMID8253795
26	RHO (c.632A>C:p.His211Pro)	IIa	PMID8253795
27	RHO (c.50C>T:p.Thr17Met)	IIa	PMC52606
28	RHO (c.50C>T:p.Thr17Met)	IIa	PMC52606
29	RHO (c.404_405delinsGG>TT:p.Arg135Leu)	III	PMC437971
30	RHO (c.68C>A:p.Pro23His)	IIa	PMC52606
31	RHO (c.68C>A:p.Pro23His)	IIa	PMC52606
32	RHO (c.68C>A:p.Pro23His)	IIa	PMC52606
33	RHO (c.68C>A:p.Pro23His)	IIa	PMC52606
34	RHO (c.68C>A:p.Pro23His)	IIa	PMC52606
35	RHO (c.68C>A:p.Pro23His)	IIa	PMC52606
36	RHO (c.403C>T:p.Arg135Trp)	III	PMC437971
37	RHO (c.1040C>T:p.Pro347Leu)	I	PMC52606
38	RHO (c.1040C>T:p.Pro347Leu)	I	PMC52606

RHO = rhodopsin; - = mutation class unknown

Image acquisition and measurements

Imaging was conducted after adequate pupil dilation (>7 mm) using phenylephrine hydrochloride (2.5%) and tropicamide (1%). Fundus autofluorescence (FAF, 488 nm excitation) and horizontal 9 mm SD-OCT images at the fovea were acquired using the Spectralis HRA+OCT (Heidelberg Engineering, Heidelberg, Germany) at each visit. OCT imaging was assisted by eye-tracking technology that enables accurate and reproducible scans at the same location on the fovea across multiple visits. The images were recorded with a 30-degree field of view; in cases where the rings were too large to be visualized with the 30-degree field of view, scans with a 55-degree field of view were also captured.

The ellipsoid zone line widths, and horizontal and vertical diameters of the hyperautofluorescent ring were manually measured using the built-in measuring tool provided by the Spectralis software. The ellipsoid zone line width was measured between the nasal and temporal limits of the ellipsoid zone layer using the horizontal foveal scan on SD-OCT. The external border of the hyperautofluorescent ring was used to determine diameter length, as it is more clearly defined and easily visualized compared to the internal border. The horizontal diameter is oriented along the axis formed by the center of the fovea and the center of the optic disc. The vertical diameter is defined as the length of the line between the external ring border, perpendicular to the horizontal

diameter and passing the center of the fovea (Figure 3). For each parameter (ellipsoid zone line width, horizontal and vertical diameters of the autofluorescent ring), two measurements were taken by the author (L.C.) four weeks apart for each studied image in order to assess for test-retest reliability. Cystoid macular edema (CME) was also noted if it significantly present in the OCT images. The hyperautofluorescent rings seen on FAF were qualitatively categorized as either typical (uniformly round, ellipsoidal rings) or atypical (any ring that deviates from the typical morphology). Figure 4 shows an example of typical vs. atypical ring morphology.

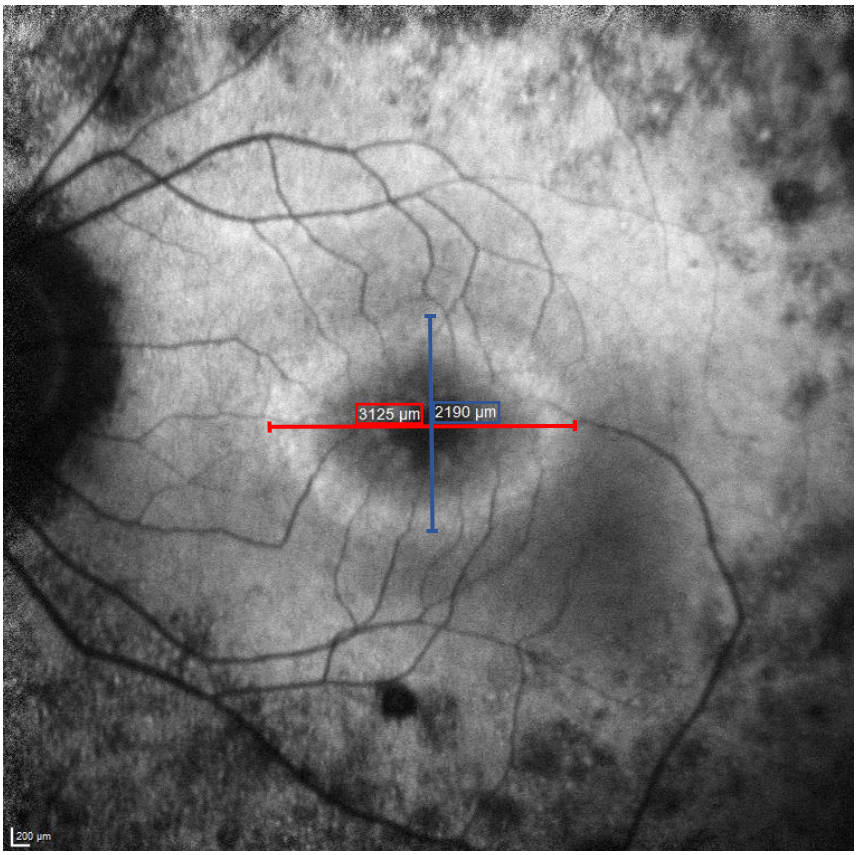

Figure 3. Short wavelength fundus autofluorescence (SW-FAF) image of left eye. Red: horizontal diameter measurement; blue: vertical diameter measurement.

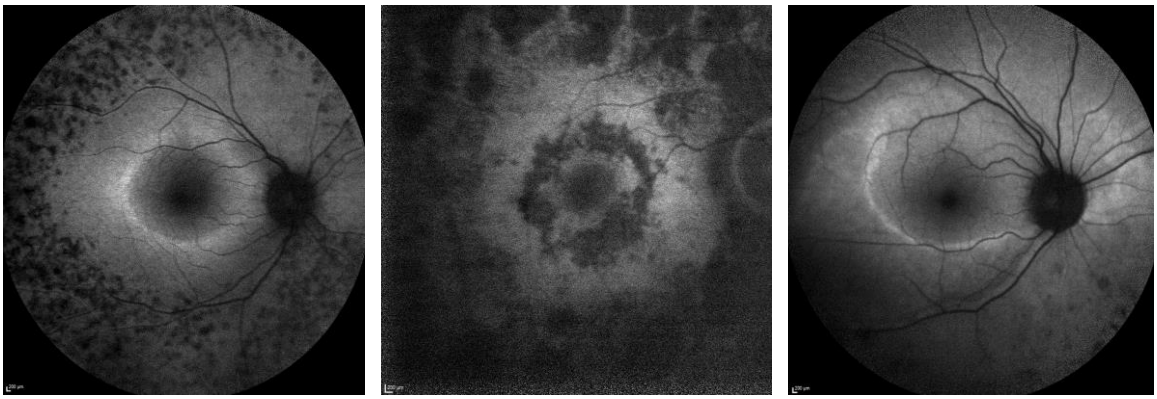

Figure 4. Examples of various forms of hyperautofluorescent ring morphology on fundus autofluorescence (FAF) imaging. Left: typical, uniformly round, ellipsoidal ring. Middle: atypical, irregularly shaped autofluorescence surrounded by regions of atrophy. Right: atypical, arcuate autofluorescence in the inferior macula.

Electroretinography

Full-field electroretinography (ffERG) was performed using disposable corneal low-impedance corneal DTL electrodes and the Diagnosys Espion Electrophysiology System (Diagnosys LLC, Lowell, MA, USA) on both eyes in accordance to the International Society for Clinical Electrophysiology of Vision (ISCEV) standards. Dark-adapted 0.01 cd·s·m^-2 stimulus strength (rod response), dark-adapted 3.0 cd·s·m^-2 (combined rod-cone response), light-adapted 3.0 cd·s·m^-2 (single-flash cone response), and light-adapted 3.0 cd·s·m^-2 flicker (30 Hz flicker) ERG recordings were obtained. The patients were dark-adapted for a minimum of 20 minutes before the scotopic ERG measurements and were light-adapted for a minimum of 10 minutes prior to the photopic ERG tests. For patients with 30 Hz flicker amplitudes less than 5 uV or who were predicted to have less than 5 uV based on clinical examination, bipolar

Burian-Allen contact lens electrodes were used with narrow bandpassed filtering and computed averaging in order to minimize electrical artifacts and noise when measuring small amplitude cone responses (52). The 30 Hz flicker data were used for analysis as it is a commonly used outcome measure of visual function in RP patients (52). Because rod function is usually the first to be affected in RP, the scotopic ERG responses are typically markedly diminished at presentation, making the 30 Hz flicker cone ERG response (Figure 5) a useful prognostic marker of functional vision in everyday activities.

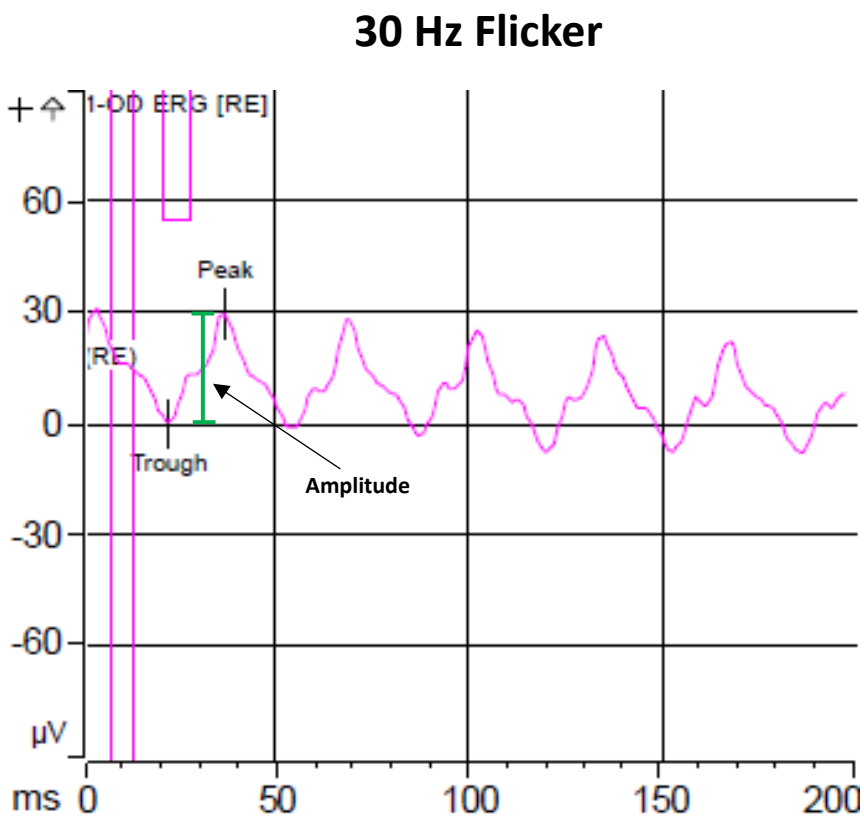

Figure 5. 30 Hz flicker waveform with peak, trough, and amplitude marked (green).

Statistical analysis

For each patient in the cohort, measurements of EZ line width and horizontal and vertical hyperautofluorescent ring diameters were obtained from SD-OCT and FAF images, respectively, from the most recent visit and the first visit if the patient was seen more than once in our clinic. The widths and diameters were measured by the author (L.C.) four weeks apart to determine test-retest reliability. The intraclass correlation coefficient (ICC) was calculated for each structural parameter to determine the reliability of the test-retest measurements. To calculate the correlation between each pair of parameters, the Pearson correlation coefficient was used based on the average of the two test-retest measurements. The rate of progression was calculated for each parameter by taking the difference between the value from the most recent visit and the value from the first visit, divided by the length of follow-up. In order to test for symmetry of the right and left eyes (i.e., whether the progression rates of the right and left eyes were similar), the difference in progression rates between the eyes was compared to the variability of test-retest measurements of the right eye. All statistical analyses were performed using Stata 12.1 (StataCorp LP, College Station, TX).

Results

Clinical data

A total of 38 patients were identified as having adRP caused by mutations in the *RHO* gene. 11 patients were excluded from the study as a result of having advanced-stage disease with no visible EZ line at any time point, leaving 27 patients in our analysis. Sixteen (59.3%) patients were female and eleven (40.7%) were male. The average age of patients at the initial visit was 44.0 years (standard deviation 17.7 years, range 15-78 years). Sixteen patients had measurements from more than one clinic visit, while eleven patients were examined at only one clinic visit and thus did not receive any analysis for disease progression. The age distribution of patients with data from multiple clinical visits is shown in Table 3. The average length of follow-up for patients with more than one visit was 4.3 years (standard deviation 2.8 years). A total of 20 patients had typical symmetric ellipsoid-shaped hyperautofluorescent rings, and 7 had atypical rings that deviated from the typical morphology. Six patients were observed to have cystoid macular edema (CME) in either eye. The results are summarized in Table 4.

Table 3: Age distribution of subjects with multiple clinical visits

n	Mean age (years)	Standard deviation	Quantiles				
			Minimum	25th	Median	75th	Maximum
16	43.6	19.4	15	25.5	43.5	57.5	78

Table 4. Genotype, demographic, and clinical characteristics of study subjects

ID	Age	Sex	Genotype	Years of follow-up	Typical ellipsoidal hyperautofluo-rescent ring	Muta-tion class	CME
1	23	F	RHO (c.937-27_-19delCCCTGACTC)	6.8	+	I	
2	71	M	RHO (c.946delT:p.Cys316Alafs*44)			N/A	+
3	44	F	RHO (c.266G>A:p.Gly89Asp)	0.5	+	IIb	+
4	46	F	RHO (c.328T>C:p.Cys110Arg)	2.8	+	N/A	
5	16	F	RHO (c.328T>C:p.Cys110Arg)	2.8	+	N/A	
6	69	F	RHO (c.328T>C:p.Cys110Arg)	6.4		N/A	
7	15	M	RHO (c.568G>A:p.Asp190Asn)	3	+	IIa	
8	59	M	RHO (c.568G>A:p.Asp190Asn)	7	+	IIa	
9	43	M	RHO (c.266G>Ap.Gly89Asp)	7		IIb	+
10	56	F	RHO (c.1025G>A:p.Thr342Met)	8.3	+	I	
11	39	F	RHO (c.541G>A:p.Glu181Lys)	0.1		IIa	
12	66	M	RHO (c.800C>T:p.267Leu)	8	+	IIa	
13	78	M	RHO (c.316G>A:p.Gly106Arg)	5.7	+	IIb	+
14	37	F	RHO (c.404G>T:p.Arg135Leu)	3.7	+	III	
15	34	F	RHO (c.1040C>T:p.Pro347Leu)		+	I	
16	28	M	RHO (c.1040C>T:p.Pro347Leu)		+	I	
17	46	M	RHO (c.1040C>T:p.Pro347Leu)		+	I	
18	49	M	RHO (c.632A>C:p.His211Pro)		+	IIa	
19	19	M	RHO (c.50C>T:p.Thr17Met)		+	IIa	
20	28	F	RHO (c.50C>T:p.Thr17Met)	4.2	+	IIa	
21	56	F	RHO (c.404_405delinsGG>TT:p.Arg135Leu)	1.7		III	
22	37	F	RHO (c.68C>A:p.Pro23His)		+	IIa	
23	56	F	RHO (c.68C>A:p.Pro23His)		+	IIa	
24	32	F	RHO (c.68C>A:p.Pro23His)		+	IIa	
25	56	M	RHO (c.68C>A:p.Pro23His)			IIa	+
26	61	F	RHO (c.68C>A:p.Pro23His)			IIa	
27	23	F	RHO (c.1040C>T:p.Pro347Leu)	0.2	+	I	

RHO = rhodopsin; CME = cystoid macular edema; N/A = mutation class unknown; + = finding is present

Reliability of measurements

The test-retest reliability was assessed using the intraclass correlation coefficient (ICC) for each of the three measurement parameters. Within each measurement parameter, the data for both eyes at all time points were pooled. The ICC for the ellipsoid zone line width was 0.9989, ICC for the horizontal diameter was 0.9889,

and the ICC for the vertical diameter was 0.9771. Graphs showing the intraobserver reliability of the three parameters for each eye are shown in Figure 6.

To determine the strength of linear association between each of the three imaging parameters, the Pearson correlation coefficient (two-tailed, $\alpha = 0.05$) was calculated. The analysis revealed a high degree of correlation between each pair of parameters (scatterplots shown in Figure 7): $r = 0.9325$ ($p < 0.0001$) for the ellipsoid zone line and horizontal diameter measurements, $r = 0.9081$ ($p < 0.0001$) for the ellipsoid zone line and vertical diameter measurements, and $r = 0.9630$ ($p < 0.0001$) for the horizontal diameter and vertical diameter measurements.

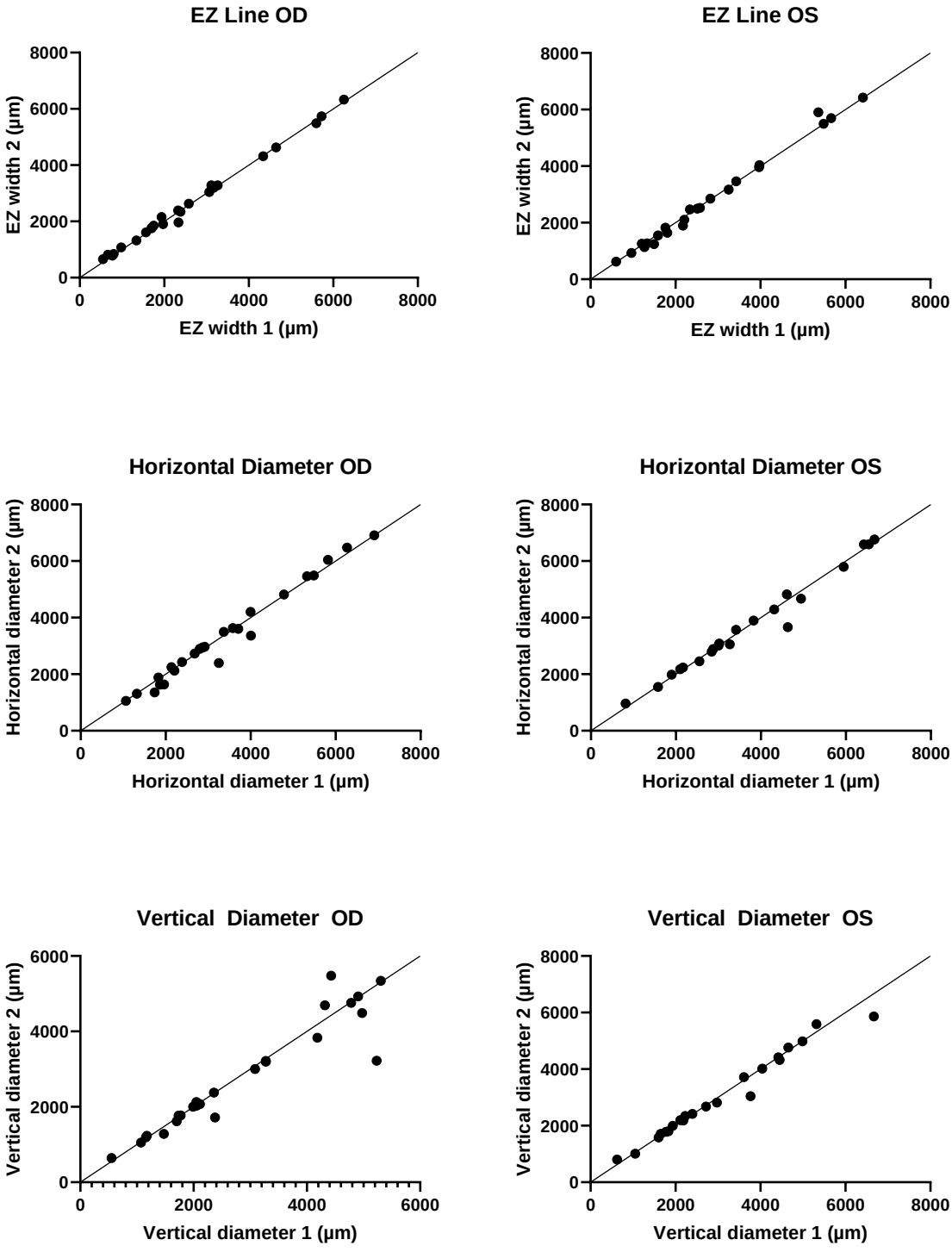

Figure 6. Intraobserver reliability of ellipsoid zone line widths, hyperautofluorescent horizontal ring diameters, and vertical ring diameters of right (OD) and left (OS) eyes in a cohort of 27 patients with autosomal dominant retinitis pigmentosa. Measurements for each parameter were taken four weeks apart. Line of equality shown.

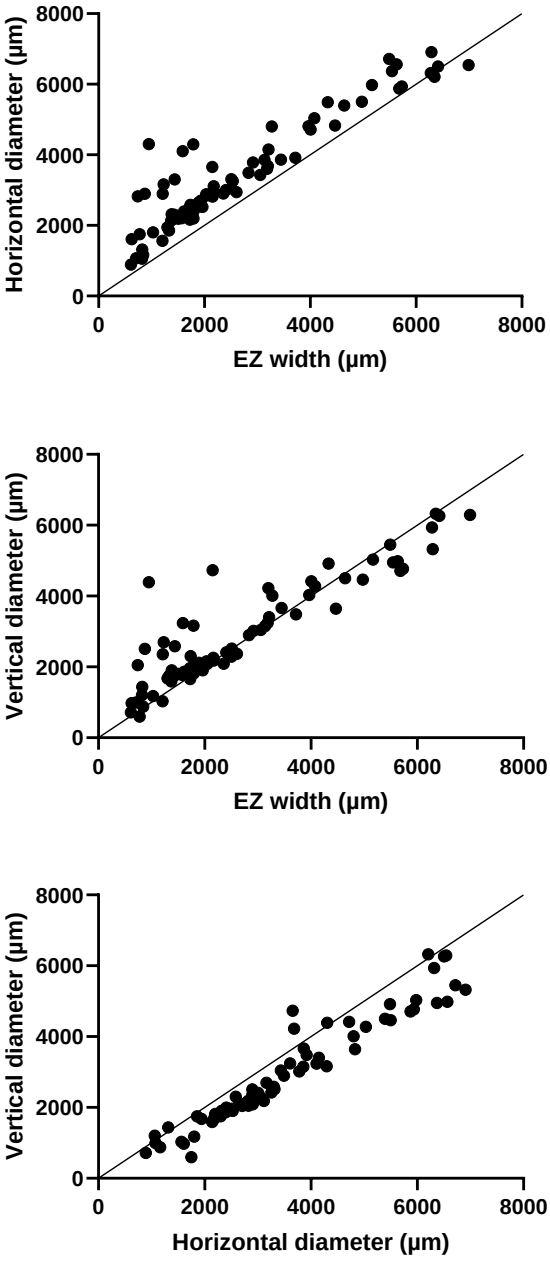

Figure 7. Correlation of ellipsoid zone line widths, hyperautofluorescent horizontal ring diameters, and vertical ring diameters. Scatterplots show EZ line widths compared to horizontal width diameters (top), EZ line widths compared to vertical diameters (middle), and horizontal diameters compared to vertical diameters (bottom).

Structural progression rate

Using the structural measurements for patients with multiple time points, the progression rate for each parameter was calculated separately for each eye (Table 5). The progression rates were calculated with *p*-values using the null hypothesis μ = 0. All progression rates were found to be negative, indicating a decline in length over time. The mean rates of decline for the EZ line in the right eye was 208.7 μm/year (standard error = 49.8, $p = 0.0008$), EZ line in the left eye was 96.6 μm/year (standard error = 37.7, $p = 0.0248$), horizontal diameter in the right eye was 109.5 μm/year (standard error = 36.2, $p = 0.0097$), horizontal diameter in the left eye was 138.1 μm/year (standard error = 46.3, $p = 0.0124$), vertical diameter in the right eye was 114.2 μm/year (standard error = 30.5, $p = 0.0025$), and vertical diameter in the left eye was 101.5 μm/year (standard error = 31.6, $p = 0.0083$). The Wilcoxon signed-rank test was also performed for each imaging parameter for each eye as an alternative to the Student's *t*-test without assuming a normal distribution for the data (Table 6).

Table 5: Progression rates of the three measured imaging parameters for each eye

Parameter	n	Mean change (μm/yr)	Standard error	Minimum (μm/yr)	Median (μm/yr)	Maximum (μm/yr)	*p*-value*
EZ line width OD	16	-208.7	49.8	-742.9	-172.8	-7.9	0.0008
EZ line width OS	13	-96.6	37.7	-365	-86.9	173.9	0.0248
Horizontal diameter OD	14	-109.5	36.2	-466.4	-76.8	72.6	0.0097
Horizontal diameter OS	12	-138.1	46.3	-445.4	-70.0	2.8	0.0124
Vertical diameter OD	14	-114.2	30.5	-411.3	-101.9	25.3	0.0025
Vertical diameter OS	12	-101.5	31.6	-386.2	-80.3	16.2	0.0083

EZ = ellipsoid zone; OD = right eye; OS = left eye; rates = μm per year; negative rate = decrease in length; positive rate = increase in length

**p*-value calculated using one-sample Student's *t*-test with null hypothesis μ = 0

Table 6: *p*-values from Wilcoxon signed-rank test of progression rates for three imaging parameters

Parameter	*p*-value*
EZ line width OD	0.0004
EZ line width OS	0.0192
Horizontal diameter OD	0.0043
Horizontal diameter OS	0.0029
Vertical diameter OD	0.0023
Vertical diameter OS	0.0047

EZ = ellipsoid zone; OD = right eye; OS = left eye
*p-value calculated using Wilcoxon signed-rank test with null hypothesis $\mu = 0$

After the rates from both eyes were pooled to obtain an overall progression rate for each measurement, the mean rate of decline for the EZ line was 158.5 µm/year (standard error = 33.4, $p < 0.0001$), horizontal diameter was 122.7 µm/year (standard error = 28.5, $p = 0.0002$), vertical diameter was 108.3 µm/year (standard error = 21.6, $p < 0.0001$) (Table 7). Converting the progression rates in terms of percentages of the mean value at the initial visit yields an average yearly progression rate (decline) of 8.4% for the ellipsoid zone line, 3.5% for the horizontal diameter, and 3.9% for the vertical diameter.

Table 7: Overall progression rates of the three measured imaging parameters, both eyes combined

Parameter	n	Mean change (µm/yr)	Standard error	*p*-value*
EZ line width	29	-158.5	33.4	<0.0001
Horizontal diameter	26	-122.7	28.5	0.0002
Vertical diameter	26	-108.3	21.6	<0.0001

EZ = ellipsoid zone; rates = µm per year; negative rate = decrease in length; positive rate = increase in length
*p-value calculated using one-sample Student's t-test with null hypothesis $\mu = 0$

Asymmetry of disease severity and progression rates between both eyes

Since some of the subjects exhibited markedly different measurements between left and right eyes at baseline, the asymmetry of disease severity and progression rate between both eyes was assessed. For ellipsoid zone measurements, we first calculated the variability of the absolute differences between the right and left eyes using the average of the two intraobserver measurements for all time points (standard deviation = 506.8 μm). Comparison of this value to the variability of the absolute differences between the test and retest ellipsoid zone measurements of the right eye for all time points (standard deviation = 46.7 μm) shows that there is a greater amount of variability between eyes than the test-retest measurements of one eye.

Next, the 95th percentile of absolute differences in EZ line progression rates between the test and retest measurements of the right eye was calculated (110.2 μm/year) in order to set the threshold for quantifying the number of patients who had significant differences in progression rates between their left and right eyes. 23% (3/13) of the subjects with progression data for both eyes were found to have absolute differences in progression rates between eyes that exceeded the 110.2 μm/year threshold.

Repeating the asymmetry analysis for the horizontal diameter measurements, we found that the variability between the right and left eyes (standard deviation

= 968.2 μm) was greater than the variability between the test and retest measurements of the right eye (standard deviation = 184.0 μm). The 95th percentile of absolute differences in horizontal diameter progression rates between the test and retest measurements of the right eye was 173.7 μm/year. 17% (2/12) of the subjects with progression data for both eyes had differences in horizontal diameter progression rates between eyes that exceeded the 95th percentile threshold.

For the vertical diameter, the variability between the right and left eyes (standard deviation = 452.0 μm) was greater than the variability between the test and retest measurements of the right eye (standard deviation = 214.9 μm). 25% (3/12) of the subjects with progression data for both eyes were found to have significantly different vertical diameter progression rates between eyes that exceeded the 95th percentile of absolute differences in progression rates between the test and retest measurements of the right eye (117.5 μm/year).

Functional progression rate

ERG data was available for ten subjects, of which three patients had longitudinal measurements from multiple visits. The average length of ERG follow-up was 2.8 years. Table 8 summarizes the 30 Hz flicker ERG test results. For the initial visit, the mean 30 Hz flicker amplitude was 22.0 μV (standard error = 7.0) in the right eye and 23.9 μV (standard error = 7.7) in the left eye. The mean change in

amplitude of the 30 Hz flicker test was an increase in 3.9 μV per year (standard deviation = 2.8 μV).

Table 8: 30-Hz flicker amplitudes for subjects with ERG data

			Time point 1		Time point 2			
ID	Age	Length of ERG follow-up (years)	OD 30 Hz-flicker amplitude (μV)	OS 30 Hz-flicker amplitude (μV)	OD 30 Hz-flicker amplitude (μV)	OS 30 Hz-flicker amplitude (μV)	OD mean change (μV per year)	OS mean change (μV per year)
1	23	6.8	31	36	40	50	1.3	2.1
6	69		0.7	0.2				
7	15		70	70				
11	39		3	2				
13	78	0.6	21	22	23	25	3.3	5
14	37		4.8	2.6				
20	28	1.1	40	42	50	45	9.1	2.7
21	56		1.5					
25	32		15	13				
29	23		33	27				

ERG = electroretinography; OD = right eye; OS = left eye; mean change was calculated only for subjects with multiple ERG time points; time point 1 = initial visit; time point 2 = most recent visit

Mutation class-specific measurements and progression rates

Subjects were classified by rhodopsin biochemical mutation class based on a literature search of their genotypes, as seen in Table 2. For the 27 subjects that were analyzed, stratification into five groups was performed: class I, class IIa, class IIb, class III, and unknown class. The mean structural measurements for each eye and time point were calculated for each mutant group, and the results are summarized in Tables 9, 10, 11, 12, 13. Using these measurements, we calculated the rate of structural progression for each eye and each mutation

class (Table 14). The overall rate of structural progression after combining both eyes was also calculated for each mutation class (Table 15).

Table 9. Class I mutation mean structural measurements, both time points

		OD			OS		
		n	Mean	SD	n	Mean	SD
EZ line width	Time point 1	3	3540.3	2464.1	3	3388.8	2564.5
	Time point 2	3	2697.8	2879.9	3	3144.8	2297.0
Horizontal diameter	Time point 1	2	4396.3	2562.2	2	4317.3	2826.7
	Time point 2	2	3740.8	3101.0	2	3718.8	30147.3
Vertical diameter	Time point 1	2	4313.3	2845.0	2	3919.0	2852.5
	Time point 2	2	2916.3	2620.9	2	2870.5	2601.5

EZ = ellipsoid zone; OD = right eye; OS = left eye; SD = standard deviation; time point 1 = initial visit; time point 2 = most recent visit. All units are in µm.

Table 10. Class IIa mutation mean structural measurements, both time points

		OD			OS		
		n	Mean	SD	n	Mean	SD
EZ line width	Time point 1	5	2276.6	1892.1	3	3539.5	3187.8
	Time point 2	5	1991.5	1675.6	3	3144.8	2971.3
Horizontal diameter	Time point 1	4	3348.0	2070.7	3	3799.0	2736.0
	Time point 2	4	2985.3	1694.2	3	3467.0	2836.9
Vertical diameter	Time point 1	4	2730.6	1795.1	3	3433.8	2671.9
	Time point 2	4	2305.5	1640.6	3	3129.5	2845.4

EZ = ellipsoid zone; OD = right eye; OS = left eye; SD = standard deviation; time point 1 = initial visit; time point 2 = most recent visit. All units are in µm.

Table 11. Class IIb mutation mean structural measurements, both time points

		OD			OS		
		n	Mean	SD	n	Mean	SD
EZ line width	Time point 1	3	2805.7	1450.8	3	2443.2	1162.7
	Time point 2	3	2192.2	766.1	3	2034.0	802.3
Horizontal diameter	Time point 1	3	4023.5	968.6	3	3444.3	421.9
	Time point 2	3	3413.5	698.2	3	3178.8	303.8
Vertical diameter	Time point 1	3	3022.5	704.0	3	2750.7	665.5
	Time point 2	3	2774.5	639.0	3	2582.7	383.0

EZ = ellipsoid zone; OD = right eye; OS = left eye; SD = standard deviation; time point 1 = initial visit; time point 2 = most recent visit. All units are in µm.

Table 12. Class III mutation mean structural measurements, both time points

		OD			OS		
		n	Mean	SD	n	Mean	SD
EZ line width	Time point 1	2	1393.3	801.5	1	1505.0	-
	Time point 2	2	899.3	1271.7	1	1569.5	-
Horizontal diameter	Time point 1	2	1920.0	856.3	1	2190.0	-
	Time point 2	2	1863.0	770.8	3	2200.5	-
Vertical diameter	Time point 1	2	1668.3	332.0	1	1805.0	-
	Time point 2	2	1687.5	437.7	1	1778.0	-

EZ = ellipsoid zone; OD = right eye; OS = left eye; SD = standard deviation; time point 1 = initial visit; time point 2 = most recent visit; - = not available. All units are in µm.

Table 13. Mean structural measurements for unknown mutation class, both time points

		OD			OS		
		n	Mean	SD	n	Mean	SD
EZ line width	Time point 1	3	2238.5	1595.9	3	2579.5	2134.7
	Time point 2	3	1679.8	1385.9	3	1896.3	1988.4
Horizontal diameter	Time point 1	3	3409.5	1437.2	3	3682.8	1578.4
	Time point 2	3	3142.0	1525.7	3	2437.0	2404.2
Vertical diameter	Time point 1	3	2794.8	1320.8	3	3029.2	1256.6
	Time point 2	3	2409.8	1451.2	1	1998.5	2015.5

EZ = ellipsoid zone; OD = right eye; OS = left eye; SD = standard deviation; time point 1 = initial visit; time point 2 = most recent visit; - = not available. All units are in µm.

Table 14. Rate of structural progression for each mutation class, right vs. left eye

		OD			OS		
	Mutation class	n	Mean	SD	n	Mean	SD
EZ line width	Class I	3	-346.7	348.1	3	22.0	135.6
	Class IIa	5	-107.2	80.15	3	-108.4	90.8
	Class IIb	3	-237.6	203.7	3	-151.3	120.1
	Class III	2	-263.4	311.1	1	17.35	-
	Unknown	3	-174.6	115.2	3	-186.7	158.8
Horizontal diameter	Class I	2	-81.8	59.2	2	-77.2	18.1
	Class IIa	4	-103.7	132.7	3	-73.0	96.2
	Class IIb	3	-246.5	219.5	3	-178.8	229.0
	Class III	2	-14.8	23.0	1	2.8	-
	Unknown	3	-62.0	32.3	3	-250.1	195.7
Vertical diameter	Class I	2	-187.2	55.7	2	-141.3	52.8
	Class IIa	4	-102.9	90.2	3	-62.3	72.3
	Class IIb	3	-169.1	217.6	3	-48.2	60.4
	Class III	2	-3.6	40.8	1	-7.3	-
	Unknown	3	-99.6	12.1	3	-198.9	170.1

EZ = ellipsoid zone; OD = right eye; OS = left eye; SD = standard deviation; time point 1 = initial visit; time point 2 = most recent visit; - = not available. All units are in µm.

Table 15. Rate of structural progression for each mutation class, all eyes

	Mutation class	n	Mean	SD	*p*-value†
EZ line width	Class I	6	-162.3	310.8	0.2569
	Class IIa	8	-107.7**	77.6	0.0057
	Class IIb	6	-194.5*	156.9	0.0289
	Class III	3	-169.8	273.3	0.3943
	Unknown	6	-180.6*	124.2	0.0162
Horizontal diameter	Class I	4	-79.5*	35.8	0.0212
	Class IIa	7	-90.6	110.2	0.0727
	Class IIb	6	-212.7	204.0	0.0511
	Class III	3	-8.9	19.7	0.5146
	Unknown	6	-156.1	162.3	0.0651
Vertical diameter	Class I	4	-164.2**	51.6	0.0079
	Class IIa	7	-85.5*	79.3	0.0290
	Class IIb	6	-108.6	157.4	0.1519
	Class III	3	-4.8	29.0	0.8004
	Unknown	6	-149.2*	120.8	0.0292

EZ = ellipsoid zone; SD = standard deviation. All units are in µm. †*p*-value calculated using one-sample Student's *t*-test with null hypothesis µ = 0. * = *p*-value < 0.05; ** = *p*-value < 0.01

Ring morphology analysis

The presence of a typical ellipsoidal ring or an atypical ring on fundus autofluorescence was noted for each patient (Table 4). The impact of the presence of a typical ring was examined by comparing the mean progression rates in the subgroup of patients with typical rings and patients with atypical rings. For ellipsoid zone line progression rates, patients with atypical rings (n = 6) had an average rate of -154.0 µm/year (standard deviation = 173.1 µm/year). Patients with a typical ring (n = 23) had a mean rate of -159.6 µm/year (standard deviation = 185.4 µm/year). A two-sample Student's *t*-test (two-tailed, equal variance) showed a *p*-value of 0.947, indicating no significant difference in the progression rates between both groups.

For horizontal diameter rates, patients with atypical ring morphology (n = 5) had a mean change of -113.5 µm/year (standard deviation = 187.8 µm/year), and those with typical ring morphology (n = 21) had an average rate of -124.9 µm/year (standard deviation = 138.7 µm/year). No significant difference in rates was found on the Student's *t*-test (*p*-value = 0.878).

Examining the vertical diameters, we found that patients with atypical rings (n = 5) had an average progression rate of -96.2 µm/year (standard deviation = 167.4 µm/year), and patients with typical rings (n = 21) progressed by -111.2 µm/year (standard deviation = 97.4 µm/year). Similar to the ellipsoid zone and horizontal diameter analyses, no significant difference in vertical diameter progression between both subgroups was found using the *t*-test (*p*-value = 0.790).

Discussion

Overall, this study of progression in retinitis pigmentosa patients with autosomal dominant rhodopsin mutations demonstrates that ellipsoid zone line widths as measured by SD-OCT and hyperautofluorescent ring diameters measured by SW-FAF can be used to detect progression in RP, corroborating previous studies of disease progression in RP cohorts with varying mean lengths of follow-up (39, 53-55). While most studies had a genetically heterogeneous group of RP patients with X-linked, syndromic, autosomal dominant, and autosomal recessive RP, this study examined only those with confirmed autosomal dominant *RHO* mutations. The mean length of follow-up for our patients was 4.3 years (SD = 2.8 years), while Sujirakul et al. had a 2-year mean follow-up, Takahashi et al. had an average follow-up of 4.5 years, and Cabral et al. had a mean length of 3.1 years (53-55). The mean rates of decline were 158.5 μm/year (8.4%) for EZ line widths, 122.7 μm/year (3.5%) for horizontal diameters, and 108.3 μm/year (3.9%) for vertical diameters, which are comparable to rates found in previous studies (39, 53-57).

Furthermore, our results show that the three structural parameters correlate well with each other ($r = 0.9325$ for EZ line and horizontal diameter; $r = 0.9081$ for EZ line and vertical diameter; $r = 0.9630$ for horizontal and vertical diameters) and have a high degree of intraobserver reliability (ICC = 0.9989 for EZ line, ICC = 0.9889 for horizontal diameter, ICC = 0.9771 for vertical diameter). These

findings confirm that structural measurements of disease progression using SW-FAF and SD-OCT imaging modalities are reliable and objective methods of assessing the patient's state of disease.

Asymmetry of progression in EZ line widths, horizontal diameters, and vertical diameters between the left and right eyes was also observed. 23% of subjects had asymmetry in EZ line progression, 17% had asymmetry in horizontal diameter progression, and 25% had asymmetry in vertical diameter progression. These rates are slightly higher than rates of asymmetry found in other studies. One study found an overall proportion of approximately 20% of patients with significant asymmetry between both eyes, though the asymmetry was seen only in EZ line progression and not in horizontal or vertical diameter progression of the ring (54). Another study of patients with Usher syndrome found only a 10% rate of hyperautofluorescent ring asymmetry (57). A possible cause for the differences in observed asymmetry may be that different forms of RP, whether by inheritance pattern or gene mutation, are more strongly associated with asymmetry than others. It has been observed that some genes (*RHO, PRPF8*) implicated in autosomal dominant RP may exhibit variable expressivity (58, 59), and we theorize that this variability may account for the asymmetry to some degree. A better understanding of asymmetry in RP patients will be needed to properly enroll subjects and monitor disease progression in future clinical trials. This is also particularly important because gene therapy trials often test

treatment in one eye while keeping the untreated eye as an internal control, and asymmetry may skew results.

Functional progression using the 30 Hz flicker amplitudes on electroretinography was also examined. The 30 Hz flicker test was chosen as a useful outcome to measure given that scotopic ERG responses are commonly extinguished in RP patients at the time of presentation. The flicker amplitudes were also used as the main outcome measure in the landmark trial studying the effects of vitamin A and E supplementation in patients with RP (60). A mean positive change (3.9 μV/year) was observed, which is unexpected as one would expect retinal function to decline over time in a fashion similar to the structural measurements. This finding is likely due to the high test-retest variability of ERG measurements (e.g., recording conditions, electrodes, operator technique), relatively stable progression of function in slow-progressing variants of RP, and our small sample size (n = 3). Of the two clinical phenotypes, our few patients with longitudinal ERG data may likely belong to the class B phenotype, characterized by slower and less severe progression of disease. Studies on different types of retinopathies have suggested that the 30 Hz flicker amplitude may be a less sensitive, highly variable signal that does not correlate well with disease severity; instead, they propose that the 30 Hz flicker implicit time may be a more reliable marker (61, 62).

RP is genetically heterogeneous with each gene being identified as having multiple possible mutations that affect gene/protein function through distinct mechanisms. Because of this, we sought to classify each subject by their rhodopsin mutation class based on their genotype and prior *in vitro* biochemical studies of rhodopsin mutants. The mean rates of structural progression were calculated for each mutant class. However, since the size of the cohort was small (n = 27), dividing the cohort further by mutation class resulted in subgroups that were even smaller, highly variable, and too underpowered for any statistically significant conclusions to be drawn from. Some of the patients (n = 3) had mutations that were still unclassified in the literature, suggesting further work to be done in studying the molecular pathogenesis of newly discovered mutations and their effects on protein structure.

In our subjects, two patterns of hyperautofluorescent rings could be discerned: typical/ellipsoidal and atypical. These regions of maximal intensity on fundus autofluorescence with 488 nm excitation are thought to correlate to areas of the retina containing an abundance of lipofuscin through active degeneration of the photoreceptors and subsequent increased phagocytosis by the RPE. Thus, the ring may mark the boundary between healthy and diseased retina, as well as the limits of the patient's visual field. 26% (7/27) of our cohort had atypical rings, and we were interested in whether the morphology of the ring was associated with the rate of progression. No statistically significant differences were found between patients with typical and atypical morphology regarding EZ line width,

horizontal diameter, and vertical diameter progression rates. The small size of the atypical ring group may have contributed to this finding; increasing the sample size in future studies would allow for better detection of differences if they do exist.

The significance of determining the progression rates in this subset of adRP patients is three-fold: 1) this data would allow clinicians to more accurately counsel patients with these specific mutations regarding their prognosis, 2) future gene therapy trials will need to have an objective baseline of natural history disease progression for patients with their target genotype in order to determine efficacy of treatment, and 3) any results from a subset of the cohort that are unexpected or deviate from the rest of the subjects may provide the basis on which to perform further studies to elucidate mechanisms of pathogenesis and other factors that influence disease severity.

Notwithstanding its potential significance, this study has certain limitations. The retrospective nature of the study may introduce selection and information biases, as well as result in heterogeneity of the types of data/measurements at our disposal. The inclusion-exclusion criteria and subsequent subgroup classification restricted the analysis to a small cohort of patients, which decreases the statistical power. Patients with severe end-stage RP were unable to be studied due to lack of a discernable EZ line on SD-OCT. Only three subjects had longitudinal ERG data, which limits any statistically significant conclusions to be

drawn regarding functional progression. The lengths of follow-up for patients with imaging data were also variable, ranging from two months to 8.3 years. Four patients had mutations that were unable to be classified by rhodopsin mutation class. Finally, the majority of subjects had typical ellipsoidal hyperautofluorescent rings, leaving only seven patients with atypical ring morphology,

Using a combination of objective measures of visual function like the ERG and non-invasive imaging modalities such as OCT and FAF has good utility in monitoring disease progression in RP. Each modality has its own set of advantages and drawbacks. For example, electrophysiology can be used to detect early-stage disease since ERG abnormalities typically precede any structural changes on funduscopic and imaging exams (63). ERGs can also be used in determining the long-term visual prognosis of RP patients from a single visit based on the amplitudes of the 30 Hz flicker test (52). However, as previously mentioned, some of the drawbacks that make it difficult to effectively implement include high sensitivity to electrical noise through electronic interference, artifacts produced through blinking and eye movements, variability of waveforms produced depending on electrode positioning, relatively long duration of exam (~30-60 minutes), and requirement of anesthesia for use in pediatric populations. On the other hand, structural imaging with OCT and FAF can provide high-resolution images of the posterior pole of the retina with a very low degree of invasiveness and minimal test-retest variability. FAF imaging can provide data about metabolism and RPE lipofuscin accumulation that may not be

visible to the naked eye on fundus examination, and OCT enables direct visualization of the EZ line, whose characteristics such as integrity, intensity, and width have been correlated with different retinal disease processes. These imaging modalities are limited by their inability to scan beyond the central retina, the requirement of an intact EZ line (precluding patients with advanced-stage disease from analysis), and lack of direct assessment of function, which is ultimately what affects quality of life for patients. Nevertheless, structural and functional tests can complement each other to provide valuable data about the retina's overall health and function.

Looking forward, this study can be the basis of follow-up studies with increased sample sizes and power. The promising field of gene therapy for the treatment of inherited retinal degenerations may finally bring treatment options to patients who are eagerly anticipating clinical trials that will first need to characterize progression rates of disease. Future studies with sufficiently large enough cohorts can utilize mixed effect models to assess the effects of other variables such as disease stage, sex, and age on disease progression. They can also continue to look for the effects of mutation class and ring morphology on rates. Although rhodopsin mutations account for a large portion of autosomal dominant RP cases, the disease is relatively rare and the specific mutations even more so. A multicenter study would help increase the cohort size and improve the statistical confidence of any analyses, although care will have to be taken to ensure standardized imaging equipment and techniques. Studies with a longer

follow-up duration would also be helpful in capturing changes in rates over more stages of disease.

References

1. Hartong DT, Berson EL, and Dryja TP. Retinitis pigmentosa. *Lancet.* 2006;368(9549):1795-809.
2. Ferrari S, Di Iorio E, Barbaro V, Ponzin D, Sorrentino FS, and Parmeggiani F. Retinitis pigmentosa: genes and disease mechanisms. *Curr Genomics.* 2011;12(4):238-49.
3. Fahim AT, Bowne SJ, Sullivan LS, Webb KD, Williams JT, Wheaton DK, et al. Allelic heterogeneity and genetic modifier loci contribute to clinical variation in males with X-linked retinitis pigmentosa due to RPGR mutations. *PLoS One.* 2011;6(8):e23021.
4. Daiger SP, Sullivan LS, and Bowne SJ. Genes and mutations causing retinitis pigmentosa. *Clin Genet.* 2013;84(2):132-41.
5. Behjati S, and Tarpey PS. What is next generation sequencing? *Arch Dis Child Educ Pract Ed.* 2013;98(6):236-8.
6. Lagnado L, and Baylor D. Signal flow in visual transduction. *Neuron.* 1992;8(6):995-1002.
7. Basinger S, Bok D, and Hall M. Rhodopsin in the rod outer segment plasma membrane. *J Cell Biol.* 1976;69(1):29-42.
8. Zhou XE, Melcher K, and Xu HE. Structure and activation of rhodopsin. *Acta Pharmacol Sin.* 2012;33(3):291-9.
9. Sullivan LS, Bowne SJ, Birch DG, Hughbanks-Wheaton D, Heckenlively JR, Lewis RA, et al. Prevalence of disease-causing mutations in families with autosomal dominant retinitis pigmentosa: a screen of known genes in 200 families. *Invest Ophthalmol Vis Sci.* 2006;47(7):3052-64.
10. Brown G, Chen DM, Christianson JS, Lee R, and Stark WS. Receptor demise from alteration of glycosylation site in Drosophila opsin: electrophysiology, microspectrophotometry, and electron microscopy. *Vis Neurosci.* 1994;11(3):619-28.
11. Murray AR, Fliesler SJ, and Al-Ubaidi MR. Rhodopsin: the functional significance of asn-linked glycosylation and other post-translational modifications. *Ophthalmic Genet.* 2009;30(3):109-20.
12. Saliba RS, Munro PM, Luthert PJ, and Cheetham ME. The cellular fate of mutant rhodopsin: quality control, degradation and aggresome formation. *J Cell Sci.* 2002;115(Pt 14):2907-18.
13. Hwa J, Garriga P, Liu X, and Khorana HG. Structure and function in rhodopsin: packing of the helices in the transmembrane domain and folding to a tertiary structure in the intradiscal domain are coupled. *Proc Natl Acad Sci U S A.* 1997;94(20):10571-6.
14. Oprian DD. The ligand-binding domain of rhodopsin and other G protein-linked receptors. *J Bioenerg Biomembr.* 1992;24(2):211-7.
15. Sung CH, Davenport CM, and Nathans J. Rhodopsin mutations responsible for autosomal dominant retinitis pigmentosa. Clustering of functional classes along the polypeptide chain. *J Biol Chem.* 1993;268(35):26645-9.
16. Sung CH, Schneider BG, Agarwal N, Papermaster DS, and Nathans J. Functional heterogeneity of mutant rhodopsins responsible for autosomal dominant retinitis pigmentosa. *Proc Natl Acad Sci U S A.* 1991;88(19):8840-4.
17. Kaushal S, and Khorana HG. Structure and function in rhodopsin. 7. Point mutations associated with autosomal dominant retinitis pigmentosa. *Biochemistry.* 1994;33(20):6121-8.
18. Noorwez SM, Kuksa V, Imanishi Y, Zhu L, Filipek S, Palczewski K, et al. Pharmacological chaperone-mediated in vivo folding and stabilization of the P23H-opsin mutant

associated with autosomal dominant retinitis pigmentosa. *J Biol Chem.* 2003;278(16):14442-50.

19. Chuang JZ, Vega C, Jun W, and Sung CH. Structural and functional impairment of endocytic pathways by retinitis pigmentosa mutant rhodopsin-arrestin complexes. *J Clin Invest.* 2004;114(1):131-40.
20. Jacobson SG, McGuigan DB, 3rd, Sumaroka A, Roman AJ, Gruzensky ML, Sheplock R, et al. Complexity of the Class B Phenotype in Autosomal Dominant Retinitis Pigmentosa Due to Rhodopsin Mutations. *Invest Ophthalmol Vis Sci.* 2016;57(11):4847-58.
21. Massof RW, and Finkelstein D. Two forms of autosomal dominant primary retinitis pigmentosa. *Doc Ophthalmol.* 1981;51(4):289-346.
22. Napier ML, Durga D, Wolsley CJ, Chamney S, Alexander S, Brennan R, et al. Mutational Analysis of the Rhodopsin Gene in Sector Retinitis Pigmentosa. *Ophthalmic Genet.* 2015;36(3):239-43.
23. Cideciyan AV, Hood DC, Huang Y, Banin E, Li ZY, Stone EM, et al. Disease sequence from mutant rhodopsin allele to rod and cone photoreceptor degeneration in man. *Proc Natl Acad Sci U S A.* 1998;95(12):7103-8.
24. Cideciyan AV, Aleman TS, Boye SL, Schwartz SB, Kaushal S, Roman AJ, et al. Human gene therapy for RPE65 isomerase deficiency activates the retinoid cycle of vision but with slow rod kinetics. *Proc Natl Acad Sci U S A.* 2008;105(39):15112-7.
25. Cideciyan AV, Jacobson SG, Beltran WA, Sumaroka A, Swider M, Iwabe S, et al. Human retinal gene therapy for Leber congenital amaurosis shows advancing retinal degeneration despite enduring visual improvement. *Proc Natl Acad Sci U S A.* 2013;110(6):E517-25.
26. Russell S, Bennett J, Wellman JA, Chung DC, Yu ZF, Tillman A, et al. Efficacy and safety of voretigene neparvovec (AAV2-hRPE65v2) in patients with RPE65-mediated inherited retinal dystrophy: a randomised, controlled, open-label, phase 3 trial. *Lancet.* 2017;390(10097):849-60.
27. MacLaren RE, Groppe M, Barnard AR, Cottriall CL, Tolmachova T, Seymour L, et al. Retinal gene therapy in patients with choroideremia: initial findings from a phase 1/2 clinical trial. *Lancet.* 2014;383(9923):1129-37.
28. Lam BL, Davis JL, Gregori NZ, MacLaren RE, Girach A, Verriotto JD, et al. Choroideremia Gene Therapy Phase 2 Clinical Trial: 24-Month Results. *Am J Ophthalmol.* 2019;197:65-73.
29. Tessitore A, Parisi F, Denti MA, Allocca M, Di Vicino U, Domenici L, et al. Preferential silencing of a common dominant rhodopsin mutation does not inhibit retinal degeneration in a transgenic model. *Mol Ther.* 2006;14(5):692-9.
30. Shaw LC, Skold A, Wong F, Petters R, Hauswirth WW, and Lewin AS. An allele-specific hammerhead ribozyme gene therapy for a porcine model of autosomal dominant retinitis pigmentosa. *Mol Vis.* 2001;7:6-13.
31. Lewin AS, Drenser KA, Hauswirth WW, Nishikawa S, Yasumura D, Flannery JG, et al. Ribozyme rescue of photoreceptor cells in a transgenic rat model of autosomal dominant retinitis pigmentosa. *Nat Med.* 1998;4(8):967-71.
32. Zhao C, Shu X, and Sun B. Construction of a Gene Knockdown System Based on Catalytically Inactive ("Dead") Cas9 (dCas9) in Staphylococcus aureus. *Appl Environ Microbiol.* 2017;83(12).
33. Kiang AS, Palfi A, Ader M, Kenna PF, Millington-Ward S, Clark G, et al. Toward a gene therapy for dominant disease: validation of an RNA interference-based mutation-independent approach. *Mol Ther.* 2005;12(3):555-61.

34. Ginsburg GS, and Phillips KA. Precision Medicine: From Science To Value. *Health Aff (Millwood).* 2018;37(5):694-701.
35. Seiple W, Clemens CJ, Greenstein VC, Carr RE, and Holopigian K. Test-retest reliability of the multifocal electroretinogram and humphrey visual fields in patients with retinitis pigmentosa. *Doc Ophthalmol.* 2004;109(3):255-72.
36. Holopigian K, Greenstein V, Seiple W, and Carr RE. Rates of change differ among measures of visual function in patients with retinitis pigmentosa. *Ophthalmology.* 1996;103(3):398-405.
37. Young B, Eggenberger E, and Kaufman D. Current electrophysiology in ophthalmology: a review. *Curr Opin Ophthalmol.* 2012;23(6):497-505.
38. Granse L, Ponjavic V, and Andreasson S. Full-field ERG, multifocal ERG and multifocal VEP in patients with retinitis pigmentosa and residual central visual fields. *Acta Ophthalmol Scand.* 2004;82(6):701-6.
39. Birch DG, Locke KG, Wen Y, Locke KI, Hoffman DR, and Hood DC. Spectral-domain optical coherence tomography measures of outer segment layer progression in patients with X-linked retinitis pigmentosa. *JAMA Ophthalmol.* 2013;131(9):1143-50.
40. Robson AG, El-Amir A, Bailey C, Egan CA, Fitzke FW, Webster AR, et al. Pattern ERG correlates of abnormal fundus autofluorescence in patients with retinitis pigmentosa and normal visual acuity. *Invest Ophthalmol Vis Sci.* 2003;44(8):3544-50.
41. Greenstein VC, Duncker T, Holopigian K, Carr RE, Greenberg JP, Tsang SH, et al. Structural and functional changes associated with normal and abnormal fundus autofluorescence in patients with retinitis pigmentosa. *Retina.* 2012;32(2):349-57.
42. Pichi F, Abboud EB, Ghazi NG, and Khan AO. Fundus autofluorescence imaging in hereditary retinal diseases. *Acta Ophthalmol.* 2018;96(5):e549-e61.
43. Sparrow JR, and Boulton M. RPE lipofuscin and its role in retinal pathobiology. *Exp Eye Res.* 2005;80(5):595-606.
44. Fleckenstein M, Charbel Issa P, Fuchs HA, Finger RP, Helb HM, Scholl HP, et al. Discrete arcs of increased fundus autofluorescence in retinal dystrophies and functional correlate on microperimetry. *Eye (Lond).* 2009;23(3):567-75.
45. Robson AG, Michaelides M, Saihan Z, Bird AC, Webster AR, Moore AT, et al. Functional characteristics of patients with retinal dystrophy that manifest abnormal parafoveal annuli of high density fundus autofluorescence; a review and update. *Doc Ophthalmol.* 2008;116(2):79-89.
46. Ramachandran R, C XC, Lee D, B CE, Locke KG, D GB, et al. Reliability of a Manual Procedure for Marking the EZ Endpoint Location in Patients with Retinitis Pigmentosa. *Transl Vis Sci Technol.* 2016;5(3):6.
47. Hood DC, Ramachandran R, Holopigian K, Lazow M, Birch DG, and Greenstein VC. Method for deriving visual field boundaries from OCT scans of patients with retinitis pigmentosa. *Biomed Opt Express.* 2011;2(5):1106-14.
48. Birch DG, Wen Y, Locke K, and Hood DC. Rod sensitivity, cone sensitivity, and photoreceptor layer thickness in retinal degenerative diseases. *Invest Ophthalmol Vis Sci.* 2011;52(10):7141-7.
49. Birch DG, Locke KG, Felius J, Klein M, Wheaton DK, Hoffman DR, et al. Rates of decline in regions of the visual field defined by frequency-domain optical coherence tomography in patients with RPGR-mediated X-linked retinitis pigmentosa. *Ophthalmology.* 2015;122(4):833-9.
50. Yang K, Farrens DL, Altenbach C, Farahbakhsh ZT, Hubbell WL, and Khorana HG. Structure and function in rhodopsin. Cysteines 65 and 316 are in proximity in a

rhodopsin mutant as indicated by disulfide formation and interactions between attached spin labels. *Biochemistry.* 1996;35(45):14040-6.

51. Karnik SS, Sakmar TP, Chen HB, and Khorana HG. Cysteine residues 110 and 187 are essential for the formation of correct structure in bovine rhodopsin. *Proc Natl Acad Sci U S A.* 1988;85(22):8459-63.
52. Berson EL. Long-term visual prognoses in patients with retinitis pigmentosa: the Ludwig von Sallmann lecture. *Exp Eye Res.* 2007;85(1):7-14.
53. Takahashi VKL, Takiuti JT, Carvalho-Jr JRL, Xu CL, Duong JK, Mahajan VB, et al. Fundus autofluorescence and ellipsoid zone (EZ) line width can be an outcome measurement in RHO-associated autosomal dominant retinitis pigmentosa. *Graefes Arch Clin Exp Ophthalmol.* 2019.
54. Sujirakul T, Lin MK, Duong J, Wei Y, Lopez-Pintado S, and Tsang SH. Multimodal Imaging of Central Retinal Disease Progression in a 2-Year Mean Follow-up of Retinitis Pigmentosa. *Am J Ophthalmol.* 2015;160(4):786-98 e4.
55. Cabral T, Sengillo JD, Duong JK, Justus S, Boudreault K, Schuerch K, et al. Retrospective Analysis of Structural Disease Progression in Retinitis Pigmentosa Utilizing Multimodal Imaging. *Sci Rep.* 2017;7(1):10347.
56. Lima LH, Burke T, Greenstein VC, Chou CL, Cella W, Yannuzzi LA, et al. Progressive constriction of the hyperautofluorescent ring in retinitis pigmentosa. *Am J Ophthalmol.* 2012;153(4):718-27, 27 e1-2.
57. Fakin A, Jarc-Vidmar M, Glavac D, Bonnet C, Petit C, and Hawlina M. Fundus autofluorescence and optical coherence tomography in relation to visual function in Usher syndrome type 1 and 2. *Vision Res.* 2012;75:60-70.
58. Vaclavik V, Gaillard MC, Tiab L, Schorderet DF, and Munier FL. Variable phenotypic expressivity in a Swiss family with autosomal dominant retinitis pigmentosa due to a T494M mutation in the PRPF3 gene. *Mol Vis.* 2010;16:467-75.
59. Kim RY, Fitzke FW, Moore AT, Jay M, Inglehearn C, Arden GB, et al. Autosomal dominant retinitis pigmentosa mapping to chromosome 7p exhibits variable expression. *Br J Ophthalmol.* 1995;79(1):23-7.
60. Berson EL, Rosner B, Sandberg MA, Hayes KC, Nicholson BW, Weigel-DiFranco C, et al. A randomized trial of vitamin A and vitamin E supplementation for retinitis pigmentosa. *Arch Ophthalmol.* 1993;111(6):761-72.
61. Pescosolido N, Fazio S, and Rusciano D. Reliability of the Implicit Time of Flicker Erg B-Wave as an Objective Diagnostic Tool for Retinopathies. *JSM Biotechnol Bioeng.* 2014;2(2):1037.
62. Satoh S, Iijima H, Imai M, Abe K, and Shibuya T. Photopic electroretinogram implicit time in diabetic retinopathy. *Jpn J Ophthalmol.* 1994;38(2):178-84.
63. Whatham AR, Nguyen V, Zhu Y, Hennessy M, and Kalloniatis M. The value of clinical electrophysiology in the assessment of the eye and visual system in the era of advanced imaging. *Clin Exp Optom.* 2014;97(2):99-115.